*Journal of Zhejiang University-SCIENCE A (Applied Physics & Engineering) in press*
www.jzus.zju.edu.cn; www.springer.com/journal/11582
E-mail: jzus_a@zju.edu.cn

**Research Article**

https://doi.org/10.1631/jzus.A2300373

# A novel shear damage model of the shear deformation and failure process of gas hydrate-bearing sediments

Hui WANG[1,2], Bo ZHOU[1]✉

[1]*College of Pipeline and Civil Engineering, China University of Petroleum (East China), Qingdao, China*
[2]*Institute of Water Engineering Sciences, Wuhan University, Wuhan, China*

**Abstract:** A novel shear damage model based on homogenization theory and a modified Mohr-Coulomb criterion is proposed to predict the full deformation process of gas hydrate-bearing sediments (GHBS) during shearing by analyzing micro-mechanisms of shear deformation and failure characteristics. Then, the physical significance of the model's parameters is explored. Finally, the damage evolution and shear stress partition inside GHBS during the shearing process are analyzed in detail. The results show that model parameters have clear physical meaning, and the shear damage model is capable of reflecting the nonlinear deformation and strain softening characteristics of GHBS due to its ability to better describe the damage evolution and shear stress partition mechanisms inside GHBS during the shearing process. Comparisons of experimental and theoretical results show that the global performance of the novel shear damage model is satisfactory. The model is expected to be widely adopted to analyze submarine landslide instability due to hydrate dissociation.

**Key words:** Gas hydrate-bearing sediments (GHBS); Shear damage model; Homogenization theory; Modified Mohr-Coulomb criterion; Damage evolution

## 1 Introduction

Gas hydrate (GH) is commonly found in permafrost layers and deep sea beds (Stern et al., 1997; Kvenvolden, 1999; Sloan, 2003; Brugada et al., 2010). As the most promising clean energy source for the future, the safe extraction of gas hydrate has drawn increasing interest from all over the world (Yang et al., 2014). However, excessive dissociation of gas hydrate in the pore spaces of the sediment matrix due to the use of immature exploitation technology may lead to submarine landslide and wellbore collapse (Jia et al., 2016; Zhu et al., 2017). Furthermore, the escape of methane gas that is 20-30 times more potent as a greenhouse gas than $CO_2$ from hydrate reservoirs may contribute to global warming, which could lead to an increase in sea water temperatures. Further temperature increases will further promote ice melting and methane hydrate dissociation, with a significant influence on the global carbon cycle and climate change (Farahani et al., 2021a and 2021b).

In the past decade, most research has focused on the effect of the degree of saturation of GH (Masui et al., 2005; Miyazaki et al., 2010), effective confining pressure (Yu et al., 2011), strain rate (Deusner et al., 2019), GH morphology (Hyodo et al., 2013), temperature (Song et al., 2016; Liu et al., 2017), pore pressure (Hyodo et al., 2013), fine-grained content (Li et al., 2019; Hyodo et al., 2017), sediment types (Kajiyama et al., 2017; Yun et al., 2007) and hydrate dissociation (Luo et al., 2020; Hyodo et al., 2014) on the peak strength and deformation characteristics of GH-bearing sediments. These studies have involved carrying out a series of triaxial compression tests, direct shear tests, and plane strain tests. With the continuous development of laboratory visualization technology, the microstructural evolution under loading and environmental conditions has been more comprehensively studied using X-ray CT (Wu et al., 2020; Yoneda et al., 2016), MRI (Song et al., 2015; Ji et al., 2019) and Cryo scanning electron microscopy (Hou et al., 2018). Meanwhile, the discrete element

✉ Bo ZHOU, zhoubo@upc.edu.cn

Received July 21, 2023; Revision accepted Dec. 2, 2023; Crosschecked

method (DEM) was introduced to explore mesoscopic deformation and particle-scale motion from a microscopic perspective (Xu et al., 2016; Jiang et al., 2014, 2019).

Based on a large number of experimental and DEM simulation findings, several constitutive models were proposed to describe the nonlinear and strain-softening characteristics of GHBS. Many attempts have been made to capture the unique mechanical characteristics of GHBS, which are regarded as homogeneous and isotropic geotechnical materials. The models used include the Duncan-Chang model (Miyazaki et al., 2012; Yan et al., 2017), Mohr-Coulomb plastic model (Pinkert et al., 2015, 2017), critical state model (Uchida et al., 2016; Zhou et al., 2018), state-dependent constitutive model (Ng et al., 2020 and 2023; Shen et al., 2016; Fang et al., 2022), granular thermodynamic model (Bai et al., 2023) and hypoplastic model (Zhang et al., 2017). Note that these constitutive models were proposed from a phenomenological perspective, which cannot explain the microscopic mechanisms of the failure and deformation of GHBS. In contrast, some researchers considered GHBS as a composite geomaterial consisting of sediment matrix, GH particles, pore fluid, and methane gas. Hence, by hypothesizing that the external loading of hydrate-bearing sediments is jointly carried by two components, namely the sediment matrix and methane hydrate, a stress partition constitutive framework for methane hydrate-bearing sediments (SPF-MHBS) was established based on the concept of stress partition (Wang et al., 2023; Xu et al., 2023). Zhang et al. (2022) proposed a mesoelastic-plastic damage mechanical model for MHBS by introducing statistical damage theory and Gurson plastic damage theory and considering various hydrate growth patterns. Although the above meso-mechanical constitutive models of GHBS can better model the mesoscopic structural evolution under loading, there is an accompanying increase in the number of model parameters, some of which lack a physical meaning. Submarine landslides are a progressive failure process, which is accompanied by strain hardening after yielding and post-peak softening characteristics (Skempton, 1985). Hence, to rapidly evaluate the instability of submarine slopes due to gas hydrate dissociation, it is more important to establish a shear model that can describe the shear stress-shear displacement curves, including the full shear deformation and failure process. There was no relevant theory of the shear model for GHBS, and so this was an essential motivation for this study.

In this paper, the characteristics and micro-mechanism of shear deformation of GHBS in direct shear tests are summarized first. A shear damage model based on homogenization theory and a modified Mohr-Coulomb criterion is proposed to predict the shear stress-shear displacement curves of GHBS in the direct shear tests. Then, the physical significance of the shear damage model parameters is investigated. Finally, the novel shear damage model is used to describe the evolution of damage and shear stress partition mechanisms inside GHBS.

## 2 Characteristics and micro-mechanism of shear deformation

GH-bearing sediments (Fig. 1), are composed of GH particles, sand particles, methane gas, and water. Therefore, the mechanical characteristics of the microscopic components and the interaction between them predominantly determine the macroscopic mechanical behavior of the sediments. Fig. 2 depicts a typical diagram of shear stress-shear displacement of GHBS, which may be divided into five stages:

(1) Elastic deformation stage (stage OA): in the early stages of OA, shear stress increases linearly with increasing displacements. As a result, the deformation at this stage is categorized as elastic deformation. The macroscopic phenomena are explained by the absence of hydrate bond breakage at the particle scale.

(2) Yield hardening stage (Stage AB): after passing over point A, the shear stress curve becomes convex rather than straight. Point A, the initial yield point, represents the transition from the elastic stage to the plastic hardening stage. This occurs because hydrate bonds break occur at random in GHBS under external stress, resulting in slipping and rotation of sand particles.

(3) Strain softening stage (stage BC): after the peak strength point (corresponding to point B), with an increase in displacement, shear stress decreases rapidly from peak strength to residual strength. The loss of cohesion strength inside sediments, which results from breakage of hydrate bonding, is the primary cause of a decrease in shear strength (strain softening).

(4) Residual strength stage (stage CD): when shear stress reaches this point, which is independent of displacement, it remains constant. The constant shear stress during the stage is defined as the residual strength. From a microscopic perspective, friction at the interface between hydrate particles and sand particles contributes to the residual strength of GH-bearing sediments.

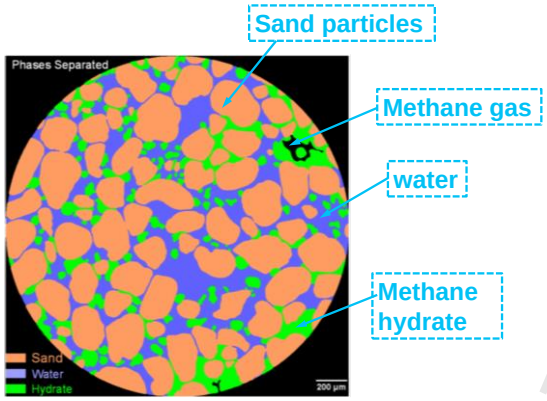


**Fig. 1 CT results of gas hydrate-bearing sediments (modified from Lei et al., 2019).**

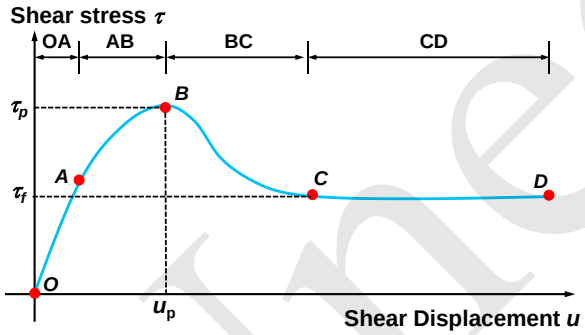


**Fig. 2 Representative shear constitutive relationship of GHBS (Liu et al., 2017 and 2018).**

Table 1 depicts particle-scale mechanisms of GHBS with different saturations under shearing. As hydrate saturation increases, hydrates have various effects on the sliding and rotation of sand particles, resulting in an increase in the macroscopic residual strength of GH-bearing sediments. Also, the hydrate pore morphology plays a different role in hydrate deformation and failure. When the hydrate saturation is less than 25%, the hydrate mostly fills the pores in a pore-filling type, which increases the shear strength of GHBS by increasing the frictional resistance of sand particle surfaces. When the hydrate saturation is greater than 40%, the hydrate in the pore spaces is mostly in the form of cementation and grain coating, which mainly increases the shear strength and resistance to deformation by cementing the neighboring sand particles and increasing the friction on the surface of sand particles. In a permafrost region, the presence of ice can cement two adjacent sand particles together to form stronger cemented clusters, thereby giving the hydrate reservoir a higher strength. At the same time, although gas hydrates are more stable at high pressures, ice will be melted at high pressures, which also leads to more settlement deformation of hydrate reservoirs in permafrost regions.

**Table 1 Particle-scale mechanisms of GHBS under shearing (modified from Yun et al., 2007; Liu et al., 2017).**

| $S_{MH}$ | Initial states | Mechanism in movement | |
|---|---|---|---|
| 0% |  Initial |  Slip |  Rotation |
| < 25% Pore filling |  Initial |  Slip |  Rotation |
| >40% Grain coating |  | 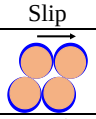 |  |
| >40% Cementing |  Initial |  Slip |  Rotation |

## 3. Shear damage model for GHBS

### 3.1 Basic concepts

GH-bearing sediments are composite geotechnical materials composed of sediment matrix particles (sand or clay particles), hydrate particles, water, and free methane gas, resulting in complex physical and mechanical characteristics (Lei et al., 2019; Wu et al., 2023). Previous findings have demonstrated that GH particles are mainly bonded and bridged between the sand particles (Chaouachi et al., 2015; Li et al., 2019). The presence of natural GH particles results in stronger structural characteristics of sediments. When GHBS are subjected to external loadings, bond breakage between the GH particles and sand particles gradually occurs. Therefore, GH-bearing sediments are divided into two parts: intact parts, called bonded elements, and damaged parts, called frictional elements (Fig. 3) (Zou et al., 2020). The essence of the

evolution of the macroscopic mechanical response of GHBS is the result of a decrease in the number of bonded elements and an increase in the number of frictional elements inside the sediments. In this study, bonded elements were considered as elastic brittle materials, whereas frictional elements were seen as ideal elastic-plastic materials (Fig. 4) (Xie et al., 2020a and 2020b).

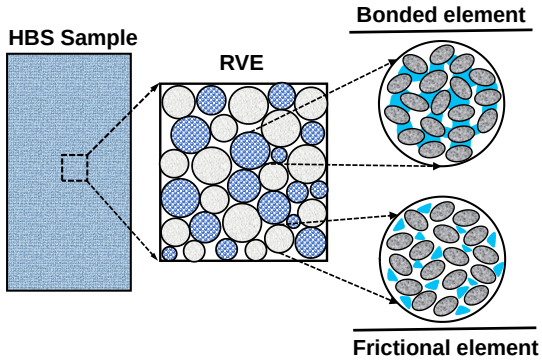


**Fig. 3 Structure model of gas hydrate-bearing sediments.**

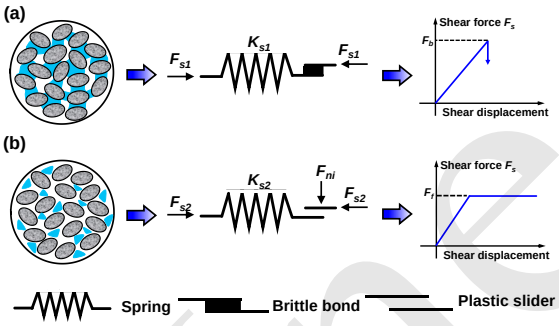


**Fig. 4 Mechanical response of RVE: (a) Bonded elements; (b) Frictional elements.**

Total shear force $\boldsymbol{T}$ on the shear surface may be expressed using binary medium theory (Zou et al., 2020):

$$\boldsymbol{T}=\left[\sum_{i=1}^{N_b}\left(k_b+k_f\right)\boldsymbol{u}+\sum_{i=1}^{N_f}\boldsymbol{P}_{ni}\tan\phi_i\right]*A \quad (1)$$

where $A$ is the area of the shear surface; $k_b$ and $k_f$ are the shear stiffnesses of the bonded elements and frictional elements, respectively; $\phi_i$ is the friction angle of the frictional elements; and $\boldsymbol{P}_{ni}$ is the normal stress of frictional elements. $N_b$ and $N_f$ denote the number of bonded elements and frictional elements, respectively. Then, the average shear stress $\tau$ on the shear surface can be obtained by dividing both sides by $A$, as shown in Eq. (2):

$$\boldsymbol{\tau}=\left[\sum_{i=1}^{N_b}\left(k_b+k_f\right)\boldsymbol{u}+\sum_{i=1}^{N_f}\boldsymbol{P}_{ni}\tan\phi_i\right] \quad (2)$$

$D$, a damage variable to characterize the degree of structural deterioration, is defined as the ratio of the number of frictional elements to the total number of microelements:

$$D=\frac{N_f}{N_{total}} \quad (3)$$

where $N_f$ denotes the number of frictional elements and $N_{total}$ the total number of microelements. When Eq. (3) is substituted into Eq. (2), we obtain:

$$\tau=\tau_b\left(1-D\right)+D\tau_f \quad (4)$$

where $\tau_b$ and $\tau_f$ are the shear stress of bonded elements and frictional elements respectively. Substituting $\tau_b=k_{HBS}u$ into Eq. (4) yields the shear constitutive relationship

$$\tau=k_{HBS}u\left(1-D\right)+D\tau_f \quad (5)$$

where $k_{HBS}$ is the initial shear stiffness of GH-bearing sediments.

### 3.2 Damage evolution equation

Research has shown that the strain-softening characteristics of GHBS are directly related to bond breakage between GH particles and sand particles (Wu et al., 2020; Wang et al., 2021). Therefore, the determination of the damage evolution law inside sediments was critical for predicting the accuracy of the constitutive model proposed in the present study. The application of probabilistic methods to describe the damage evolution of geomaterials is now widely accepted. Lai et al. (2008) discovered that the Weibull distribution could more accurately describe the strength distribution of frozen soil than other probabilistic methods. As a result, the Weibull function was used to quantify the progression of damage inside GHBS. The Weibull distribution's probability density function $P(F_a)$ is expressed as follows (Hallinan, 1993):

$$P\left(F_a\right)=\frac{m}{F_0}\left(\frac{F_a}{F_0}\right)^{m-1}\exp\left[-\left(\frac{F_a}{F_0}\right)^m\right] \quad (6)$$

where $F_a$ denotes the micro-element strength distribution variable and $F_0$ and m represent the model parameters of the Weibull function. When the stress level $F$ is reached, the number of damaged micro-elements $N_f$ may be stated as:

$$N_{\mathrm{f}}=\int N_{\mathrm{total}}P(F_{\mathrm{a}})dF=N_{\mathrm{total}}\left\{1-\exp\left[-\left(\frac{F_{\mathrm{a}}}{F_0}\right)^{\mathrm{m}}\right]\right\} \tag{7}$$

The expression of the statistical damage variable $D$ can be obtained by solving the simultaneous equations Eq. (6) and Eq. (7):

$$D=\frac{N_{\mathrm{f}}}{N_{\mathrm{total}}}=1-\exp\left[-\left(\frac{F_{\mathrm{a}}}{F_0}\right)^{\mathrm{m}}\right] \tag{8}$$

Eq. (8) is the damage evolution equation of GHBS.

### 3.3 Determining the strength criterion of micro-elements

The failure criterion of GHBS can be expressed by the general formula:

$$F_{\mathrm{a}}=f(\tau)-K_0=0 \tag{9}$$

where $\tau$ is shear stress and $K_0$ is a constant related to material properties. As the external loading increases, the stress state inside the GHBS changes continuously. If $f(\tau) > K_0$, it implies that the micro-elements of GHBS have been damaged. The strength criterion, which is used to determine the micro-element strength $F$ of GHBS, is the key to determining the damage variable $D$. Due to its simple parameters, and extensive application in engineering, the Mohr-Coulomb (MC) criterion has been adopted to predict the strength of GHBS with different hydrate saturation levels (Dong et al., 2020). Its expression is as follows:

$$F_{\mathrm{a}}=\tau-\tau^{y}=\tau-\left(\sigma_{\mathrm{n}}\tan\varphi_{\mathrm{HBS}}^{\mathrm{y}}+c_{\mathrm{HBS}}^{\mathrm{y}}\right) \tag{10}$$

where $\sigma_{\mathrm{n}}$ denotes the normal stress and $\varphi_{\mathrm{HBS}}^{\mathrm{y}}$ and $c_{\mathrm{HBS}}^{\mathrm{y}}$ represent the frictional angle and cohesion in the yield state for GHBS, respectively. Substituting Eq. (10) into Eq. (8), the specific form of the damage evolution equation can be obtained as:

$$D=\frac{N_{\mathrm{f}}}{N_{\mathrm{total}}}=\begin{cases}0, & u<u^{\mathrm{y}}\\ 1-\exp\left[-\left(\dfrac{ku-\sigma_{\mathrm{n}}\tan\varphi_{\mathrm{HBS}}^{\mathrm{y}}-c_{\mathrm{HBS}}^{\mathrm{y}}}{F_0}\right)^{\mathrm{m}}\right], & u\ge u^{\mathrm{y}}\end{cases} \tag{11}$$

where $u^{\mathrm{y}}$ denotes the shear displacement corresponding to the initial yield point. By substituting Eq. (11) into Eq. (5), the shear constitutive model of GHBS can be expressed as follows:

$$\tau=\begin{cases}k_{\mathrm{HBS}}u\exp\left[-\left(\dfrac{k_{\mathrm{HBS}}u-\sigma_{\mathrm{n}}\tan\varphi_{\mathrm{HBS}}^{\mathrm{y}}-c_{\mathrm{HBS}}^{\mathrm{y}}}{F_0}\right)^{\mathrm{m}}\right]+\\ \tau_{\mathrm{f}}\left\{1-\exp\left[-\left(\dfrac{k_{\mathrm{HBS}}u-\sigma_{\mathrm{n}}\tan\varphi_{\mathrm{HBS}}^{\mathrm{y}}-c_{\mathrm{HBS}}^{\mathrm{y}}}{F_0}\right)^{\mathrm{m}}\right]\right\}, & u>u^{\mathrm{y}}\\ k_{\mathrm{HBS}}u, & u\le u^{\mathrm{y}}\end{cases} \tag{12}$$

### 3.4 Derivation of model parameters

#### 3.4.1 Determination of distribution parameters

Weibull model parameters $F_0$ and $m$ cannot be obtained from experimental data. Hence, their determination plays a key role in developing a reasonable shear damage model for characterizing the full shear failure process of GHBS. In this study, the extremum approach was used to calculate the Weibull parameters $F_0$ and $m$ (Zou et al., 2020).

Eq. (12) should satisfy the following conditions:

$$\tau\big|_{u=u_{\mathrm{p}}}=\tau_{\mathrm{p}},\ \left.\frac{d\tau}{du}\right|_{u=u^{\mathrm{p}},\tau=\tau^{\mathrm{p}}}=0 \tag{13}$$

where $\tau_{\mathrm{p}}$ and $u_{\mathrm{p}}$ denote peak stress and corresponding peak displacement, respectively. Substituting Eq. (12) into Eq. (13), we obtain Eqs. (14) and (15):

$$\tau=k_{\mathrm{HBS}}u\left(1-D\big|_{u=u_{\mathrm{p}}}\right)+\tau_{\mathrm{f}}D\big|_{u=u_{\mathrm{p}}}=\tau_{\mathrm{p}} \tag{14}$$

$$\begin{aligned}\left.\frac{d\tau}{du}\right|_{u=u^{\mathrm{p}}}&=k_{\mathrm{HBS}}\left(1-D\big|_{u=u_{\mathrm{p}}}\right)+\\ &\left(\tau_{\mathrm{f}}-k_{\mathrm{HBS}}u\big|_{u=u_{\mathrm{p}}}\right)\left.\frac{\partial D}{\partial u}\right|_{u=u_{\mathrm{p}}}=0\end{aligned} \tag{15}$$

where

$$D\big|_{u=u_{\mathrm{p}}}=1-\exp\left[-\left(\frac{k_{\mathrm{HBS}}u_{\mathrm{p}}-\sigma_{\mathrm{n}}\tan\varphi_{\mathrm{HBS}}^{\mathrm{y}}-c_{\mathrm{HBS}}^{\mathrm{y}}}{F_0}\right)^{m}\right] \tag{16}$$

$$\left.\frac{\partial D}{\partial u}\right|_{u=u_{\mathrm{p}}}=\frac{mk_{\mathrm{HBS}}\left(k_{\mathrm{HBS}}u^{\mathrm{p}}-\sigma_{\mathrm{n}}\tan\varphi_{\mathrm{HBS}}^{\mathrm{y}}-c_{\mathrm{HBS}}^{\mathrm{y}}\right)^{m-1}}{F_0^m}\cdot \exp\left[-\left(\frac{k_{\mathrm{HBS}}u^{\mathrm{p}}-\sigma_{\mathrm{n}}\tan\varphi_{\mathrm{HBS}}^{\mathrm{y}}-c_{\mathrm{HBS}}^{\mathrm{y}}}{F_0}\right)^{m-1}\right] \tag{17}$$

Eq. (14) can be simplified as follows:

$$\frac{\tau^{\mathrm{p}}-\tau_{\mathrm{f}}}{\exp\left[-\left(\frac{k_{\mathrm{HBS}}u^{\mathrm{p}}-\sigma_{\mathrm{n}}\tan\varphi_{\mathrm{HBS}}^{\mathrm{y}}-c_{\mathrm{HBS}}^{\mathrm{y}}}{F_0}\right)^{m}\right]}=k_{\mathrm{HBS}}u^{\mathrm{p}}-\tau_{\mathrm{f}} \tag{18}$$

Meanwhile, Eq. (15) can also be expressed as:

$$\frac{1}{\frac{m}{F_0}\left(\frac{k_{\mathrm{HBS}}u^{\mathrm{p}}-\sigma_{\mathrm{n}}\tan\varphi_{\mathrm{HBS}}^{\mathrm{y}}-c_{\mathrm{HBS}}^{\mathrm{y}}}{F_0}\right)^{m-1}}=k_{\mathrm{HBS}}u^{\mathrm{p}}-\tau_{\mathrm{f}} \tag{19}$$

Note that the same term $k_{\mathrm{HBS}}u^{\mathrm{p}}-\tau_{\mathrm{f}}$ can be observed in Eqs. (18) and (19). Hence, Eq. (20) can be derived by combining Eqs. (17) and (18):

$$\left(\tau^{\mathrm{p}}-\tau_{\mathrm{f}}\right)\frac{m}{F_0}\left(\frac{k_{\mathrm{HBS}}u^{\mathrm{p}}-\sigma_{\mathrm{n}}\tan\varphi_{\mathrm{HBS}}^{\mathrm{y}}-c_{\mathrm{HBS}}^{\mathrm{y}}}{F_0}\right)^{m-1}=\exp\left[-\left(\frac{k_{\mathrm{HBS}}u^{\mathrm{p}}-\sigma_{\mathrm{n}}\tan\varphi_{\mathrm{HBS}}^{\mathrm{y}}-c_{\mathrm{HBS}}^{\mathrm{y}}}{F_0}\right)^{m}\right] \tag{20}$$

Eq. (18) can also be expressed as:

$$\frac{\tau^{\mathrm{p}}-\tau_{\mathrm{f}}}{k_{\mathrm{HBS}}u^{\mathrm{p}}-\tau_{\mathrm{f}}}=\exp\left[-\left(\frac{k_{\mathrm{HBS}}u^{\mathrm{p}}-\sigma_{\mathrm{n}}\tan\varphi_{\mathrm{HBS}}^{\mathrm{y}}-c_{\mathrm{HBS}}^{\mathrm{y}}}{F_0}\right)^{m}\right] \tag{21}$$

Combining with Eqs. (20) and (21), Eq. (22) can be written as follows:

$$\left(\frac{k_{\mathrm{HBS}}u^{\mathrm{p}}-\sigma_{\mathrm{n}}\tan\varphi_{\mathrm{HBS}}^{\mathrm{y}}-c_{\mathrm{HBS}}^{\mathrm{y}}}{F_0}\right)^{m-1}=\frac{F_0}{m\left(k_{\mathrm{HBS}}u^{\mathrm{p}}-\tau_{\mathrm{f}}\right)} \tag{22}$$

Eq. (21) is taken the logarithm and the following Eq. (23) can be obtained.

$$\left(\frac{k_{\mathrm{HBS}}u^{\mathrm{p}}-\sigma_{\mathrm{n}}\tan\varphi_{\mathrm{HBS}}^{\mathrm{y}}-c_{\mathrm{HBS}}^{\mathrm{y}}}{F_0}\right)^{m}=\ln\left(\frac{k_{\mathrm{HBS}}u^{\mathrm{p}}-\tau_{\mathrm{f}}}{\tau^{\mathrm{p}}-\tau_{\mathrm{f}}}\right) \tag{23}$$

Multiplying both sides of Eq. (22) by the term $\frac{k_{\mathrm{HBS}}u^{\mathrm{p}}-\sigma_{\mathrm{n}}\tan\varphi_{\mathrm{HBS}}^{\mathrm{y}}-c_{\mathrm{HBS}}^{\mathrm{y}}}{F_0}$ gives: :

$$\left(\frac{k_{\mathrm{HBS}}u^{\mathrm{p}}-\sigma_{\mathrm{n}}\tan\varphi_{\mathrm{HBS}}^{\mathrm{y}}-c_{\mathrm{HBS}}^{\mathrm{y}}}{F_0}\right)^{m}=\frac{k_{\mathrm{HBS}}u^{\mathrm{p}}-\sigma_{\mathrm{n}}\tan\varphi_{\mathrm{HBS}}^{\mathrm{y}}-c_{\mathrm{HBS}}^{\mathrm{y}}}{m\left(k_{\mathrm{HBS}}u^{\mathrm{p}}-\tau_{\mathrm{f}}\right)} \tag{24}$$

Noting that the same term is on the left side of Eqs. (23) and (24), Eq. (25) should be obtained by combining Eqs. (23) and Eq. (24):

$$\ln\left(\frac{k_{\mathrm{HBS}}u^{\mathrm{p}}-\tau_{\mathrm{f}}}{\tau^{\mathrm{p}}-\tau_{\mathrm{f}}}\right)=\frac{k_{\mathrm{HBS}}u^{\mathrm{p}}-\sigma_{\mathrm{n}}\tan\varphi_{\mathrm{HBS}}^{\mathrm{y}}-c_{\mathrm{HBS}}^{\mathrm{y}}}{m\left(k_{\mathrm{HBS}}u^{\mathrm{p}}-\tau_{\mathrm{f}}\right)} \tag{25}$$

By solving Eq. (25), the model parameter $m$ is expressed as follows:

$$m=\frac{k_{\mathrm{HBS}}u^{\mathrm{p}}-\left(\sigma_{\mathrm{n}}\tan\varphi_{\mathrm{HBS}}^{\mathrm{y}}+c_{\mathrm{HBS}}^{\mathrm{y}}\right)}{\left(\tau_{\mathrm{f}}-k_{\mathrm{HBS}}u^{\mathrm{p}}\right)\ln\left(\frac{\tau^{\mathrm{p}}-\tau_{\mathrm{f}}}{k_{\mathrm{HBS}}u^{\mathrm{p}}-\tau_{\mathrm{f}}}\right)} \tag{26}$$

Finally, the model parameter $F_0$ can be resolved by substituting Eq. (26) into Eq. (23), as given below:

$$F_0=\frac{k_{\mathrm{HBS}}u^{\mathrm{p}}-\left(\sigma_{\mathrm{n}}\tan\varphi_{\mathrm{HBS}}^{\mathrm{y}}+c_{\mathrm{HBS}}^{\mathrm{y}}\right)}{\left[-\ln\left(\frac{\tau^{\mathrm{p}}-\tau_{\mathrm{f}}}{k_{\mathrm{HBS}}u^{\mathrm{p}}-\tau_{\mathrm{f}}}\right)\right]^{\frac{1}{m}}} \tag{27}$$

### 3.4.2 Determination of strength parameters

Data from several studies suggest that GH saturation levels and stress conditions are the dominant factors that control the macroscopic mechanical behavior of GHBS (Miyazaki et al., 2010; Yu et al., 2011; Liu et al., 2018). Peak strength in this study was predicted by the modified Mohr-Coulomb strength criterion, as written in Eq. (28).

$$\tau^{\mathrm{p}}=\sigma_{\mathrm{n}}\tan\varphi_{\mathrm{HBS}}^{\mathrm{p}}+c_{\mathrm{HBS}}^{\mathrm{p}} \tag{28}$$

where $\tau^{p}$ denotes the peak shear stress, and $c_{HBS}^{p}$ and $\varphi_{HBS}^{p}$ denote the peak cohesion and peak internal frictional angle, respectively, of GHBS. In this study, the representative direct shear test data offered by Liu et al. (2018) were adopted. The relationship between

peak cohesion $c_{HBS}^{p}$, peak frictional angle $\varphi_{HBS}^{p}$, and GH saturation is presented in Figs. 5 and 6. The peak cohesion $c_{HBS}^{p}$ increases non-linearly with increasing hydrate saturation, whereas the peak friction angle $\varphi_{HBS}^{p}$ increases and then decreases as GH saturation increases, reaching a peak at a GH saturation level of 25%. Hence, through fitting the above experimental data, polynomials (29) and (30) were adopted in this study to express the cohesion and internal frictional angle as a function of GH saturation $S_{GH}$:

$$c_{HBS}^{p}=3.5S_{GH}^{2}+1.2S_{GH}+0.066 \quad (29)$$

$$\varphi_{HBS}^{p}=-115.5S_{GH}^{2}+64.2S_{GH}+34.7 \quad (30)$$

where $S_{GH}$ denotes GH saturation.

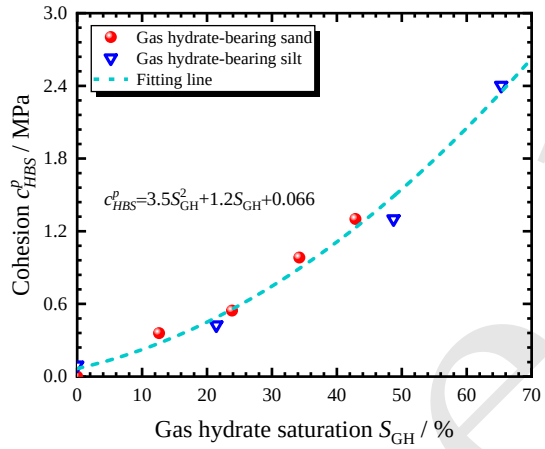


**Fig. 5 Peak cohesion .. as a function of GH saturation $S_{GH}$ (Liu et al., 2018).**

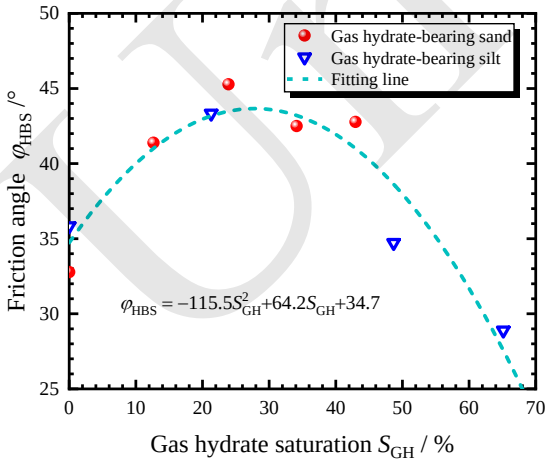


**Fig. 6 Peak frictional angle $\varphi_{HBS}$ as a function of GH saturation $S_{GH}$ (Liu et al., 2018).**

The initial yield strength was used to discern whether the bonded micro-elements of GH-bearing sediments are damaged or not (section 2.3). Therefore, determining the initial yield shear strength is fundamental for the damage evolution inside GHBS. The relationship between peak strength and initial yield shear strength of GHBS is summarized in Fig. 7. There is a clear linear relationship between initial yield strength and peak strength, which may be expressed simply as follows:

$$\tau^{y}=0.84\tau^{p}-0.1036 \quad (31)$$

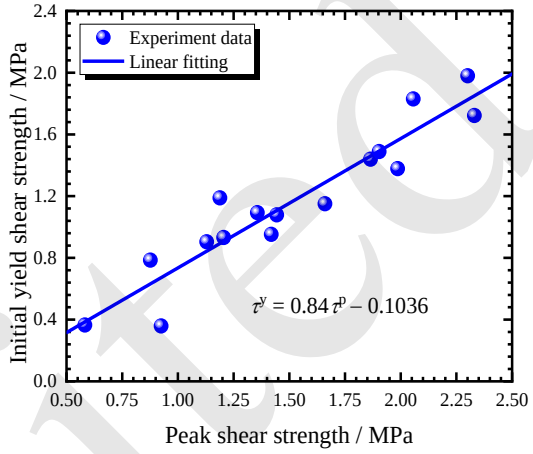


**Fig. 7 The relationship between peak strength and initial yield strength of GHBS (Liu et al., 2018).**

Fig. 8 presents the intercorrelations between the residual strength and normal pressure. Increasing normal pressure at the same GH saturation leads to an increase in the residual shear strength. The slope of the linear relationship between residual strength and normal stress gradually increases while the intercept is close to zero for sediments both with and without GH-bearing sediments. By increasing interparticle friction and rolling resistance, GH enhances the sediment's shear resistance since soil fabric and internal connectivity should have been destroyed at 100% shear strain. The residual shear strength $\tau_f$ can be calculated through Eqs. (32) and (33):

$$\tau_{f}=M\left(S_{GH}\right)\sigma_{n} \quad (32)$$

$$M\left(S_{GH}\right)=M_{0}+a_{4}S_{GH} \quad (33)$$

where $M_0$ and $a_4$ are fitting parameters; $M_0$ =0.66147, $a_4$ = 1.33788.

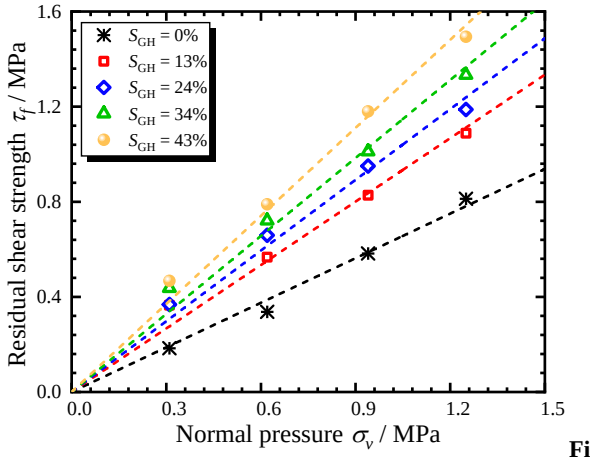


**Fig. 8 The residual shear strength versus normal pressure (Liu et al., 2018).**

## 4. Comparison of the proposed model and experimental results

In this section, the quality of the novel shear statistical damage model will be evaluated against representative direct shear test results. Liu et al. (2018) prepared synthetic GHBS samples with variable GH content. The influence of GH saturation level (13%, 24%, 34%, and 43%) and normal stress (0.31, 0.62, 0.94, and 1.25 MPa) on the mechanical characteristics and strength indices of GHBS was then investigated using a series of direct shear tests. A detailed experimental description can be found in the previous study (Liu et al., 2018).

In this study, we chose the experimental data obtained by Liu et al. (2018). The model parameters $k_{HBS}$ and $u_p$ were determined based on experimental data at various degrees of GH saturation and normal stress, while $\tau_p$ and $\tau_f$ were derived using Eqs. (27) and (31), respectively. The distribution parameters $m$ and $F_0$ were calculated by solving Eqs. (25) and (26). Table 2 shows the model parameters and methods used in this model. Tables 3-6 show the model parameters based on the direct shear testing that were used in the novel damage model of GHBS to obtain the predicted results. The validity and accuracy of the novel shear constitutive model for GHBS are validated by comparison of the predicted results with the experimental data. Fig. 9 presents the comparisons between predicted results and experimental data for GHBS under different degrees of GH saturation and normal stress. The novel shear constitutive model was able to predict the full shear deformation characteristics, especially the strain softening characteristics due to bond breakage of GH by introducing the damage mechanics. Comparison of the experimental and theoretical results in Table 7 shows that the global performance of the novel shear damage model proposed in this paper was satisfactory.

**Table 2 Model parameters and methods used in this model**

| Model parameters | Method |
|---|---|
| $k_{HBS}$ | Obtained from experimental data |
| $\tau_p$ | $\tau^p = \sigma_n \tan\varphi^p_{HBS} + c^p_{HBS}$ |
| $u_p$ | Obtained from experimental data |
| $\tau_y$ | $\tau^y = 0.84\tau^p - 0.1036$ |
| $\tau_f$ | $\tau_f = M(S_{GH})\sigma_n$ |
| | $M(S_{GH}) = M_0 + a_4 S_{GH}$ |
| $F_0$ | $m = \dfrac{k_{HBS}u^p - (\sigma_n \tan\varphi^y_{HBS} + c^y_{HBS})}{(\tau_f - k_{HBS}u^p)\ln\left(\dfrac{\tau^p - \tau_f}{k_{HBS}u^p - \tau_f}\right)}$ |
| $m$ | $F_0 = \dfrac{k_{HBS}u^p - (\sigma_n \tan\varphi^y_{HBS} + c^y_{HBS})}{\left[-\ln\left(\dfrac{\tau^p - \tau_f}{k_{HBS}u^p - \tau_f}\right)\right]^{\frac{1}{m}}}$ |

**Table 3 Model parameters for the novel shear constitutive model under normal stress of 0.31 MPa.**

| $S_{MH}$ /% | $k_{HBS}$ (MPa/mm) | $u_p$ (mm) | $\tau_p$ (mm) | $\tau_f$ (kPa) | $F_0$ | $m$ |
|---|---|---|---|---|---|---|
| 13 | 0.5675 | 1.6145 | 0.5824 | 0.385 | 1.0589 | 0.5622 |
| 24 | 1.0511 | 1.11 | 0.8763 | 0.4226 | 1.5155 | 0.8877 |
| 34 | 2.2756 | 1.0843 | 1.2053 | 0.4958 | 1.5474 | 0.7894 |
| 43 | 4.0699 | 0.7470 | 1.4438 | 0.5196 | 1.8804 | 0.7468 |

**Table 4 Model parameters for the novel shear constitutive model under normal stress of 0.62 MPa.**

| $S_{MH}$ /% | $k_{HBS}$ (kPa/mm) | $u_p$ (mm) | $\tau_p$ (mm) | $\tau_f$ (kPa) | $F_0$ | $m$ |
|---|---|---|---|---|---|---|
| 13 | 1.1720 | 2.8706 | 0.9245 | 0.72 | 0.2814 | 0.4104 |
| 24 | 1.2474 | 1.09 | 1.1887 | 0.6590 | 0.8273 | 2.5725 |
| 34 | 2.6730 | 0.84 | 1.6604 | 0.7203 | 1.8106 | 1.5239 |
| 43 | 3.2075 | 0.77 | 2.0566 | 0.7893 | 1.8919 | 2.3036 |

**Table 5 Model parameters for the novel shear constitutive model under normal stress of 0.94 MPa.**

| $S_{MH}$ /% | $k_{HBS}$ (kPa/mm) | $u_p$ (mm) | $\tau_p$ (mm) | $\tau_f$ (kPa) | $F_0$ | $m$ |
|---|---|---|---|---|---|---|

| | | | | | | |
|---|---|---|---|---|---|---|
| 13 | 0.9851 | 1.5765 | 1.1291 | 0.8003 | 0.8595 | 1.1743 |
| 24 | 1.4075 | 1.2400 | 1.3566 | 1.0088 | 0.8155 | 1.1494 |
| 34 | 2.1097 | 1.1059 | 1.9036 | 1.0398 | 1.5722 | 1.8389 |
| 43 | 4.0075 | 0.8053 | 2.3007 | 1.1522 | 2.4084 | 1.3170 |

**Table 6 Model parameters for the novel shear constitutive model under normal stress of 1.25 MPa.**

| $S_{MH}$ /% | $k_{HBS}$ (kPa/mm) | $u_p$ (mm) | $\tau_p$ (mm) | $\tau_f$ (kPa) | $F_0$ | $m$ |
|---|---|---|---|---|---|---|
| 13 | 1.1541 | 2.2951 | 1.4189 | 1.1541 | 0.6597 | 0.6188 |
| 24 | 2.6719 | 1.1944 | 1.8649 | 1.1554 | 1.7247 | 0.8548 |
| 34 | 3.2698 | 0.8360 | 1.9865 | 1.1751 | 1.6465 | 1.0972 |
| 43 | 3.4622 | 0.8025 | 2.3311 | 1.4189 | 1.5988 | 1.7361 |

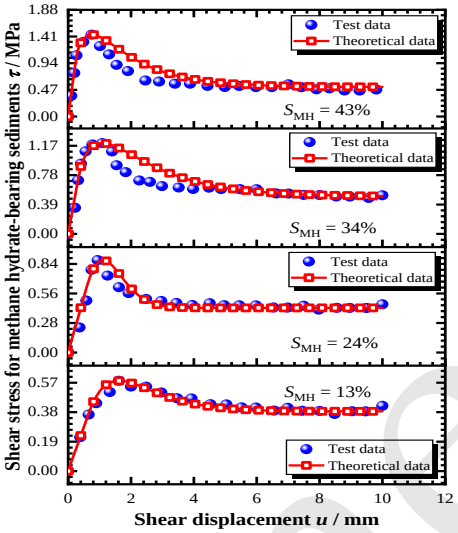


(a) Normal stress $\sigma_v = 0.31$ MPa

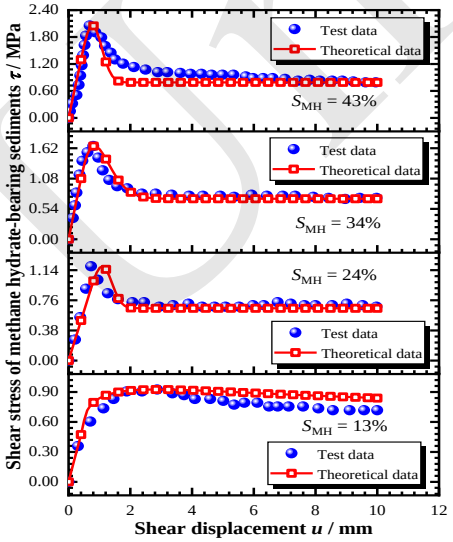


(b) Normal stress $\sigma_v = 0.62$ MPa

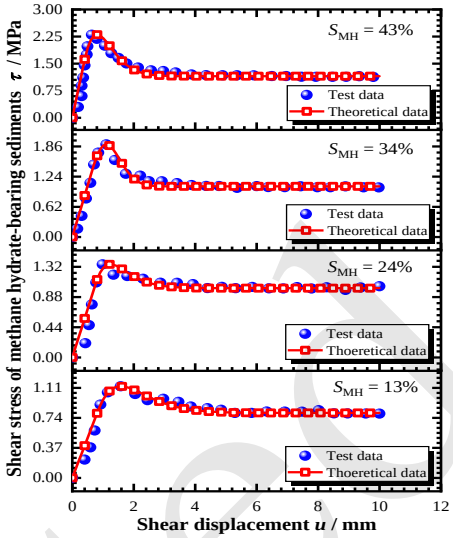


(c) Normal stress $\sigma_v = 0.94$ MPa

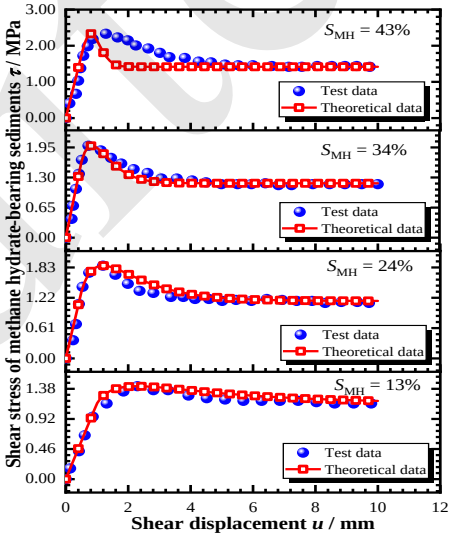


(d) Normal stress $\sigma_v = 1.25$ MPa

**Fig. 9 Comparisons between experimental and predicted results for GHBS under the different degrees of GH saturation.**

## 5. Parametric analysis

### 5.1 The influence of $F_0$

Fig. 10 depicts how the distribution parameter $F_0$ affects the damage evolution and shear stress-shear displacement curves of GH-bearing sediments. Fig. 10a demonstrates that as the distribution parameter $F_0$ increases, the peak shear stress steadily rises, but the initial stiffness and residual shear stress remain unchanged. Furthermore, the same softening rate of shear stress-shear displacement curves with different distribution parameters $F_0$ is observed, and the value

of the distribution parameter $F_0$ does not have any influence on the shape of the shear constitutive relation curves after the peak. The degree of bonding failure of GH, which is the microscopic origin of macroscopic strain softening, may be reflected in the distribution of damage within GHBS. Fig. 10b depicts the damage evolution inside GHBS with various distribution parameters $F_0$. The growth rate related to damage gradually decreases as the distribution parameter $F_0$ increases, indicating that bonding failure is less likely to occur in GH-bearing sediments with a larger model parameter $F_0$ than in those with a smaller model parameter $F_0$.

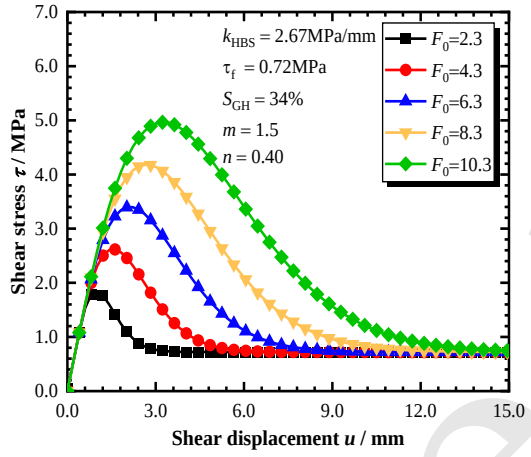


(a) Shear stress-displacement curves

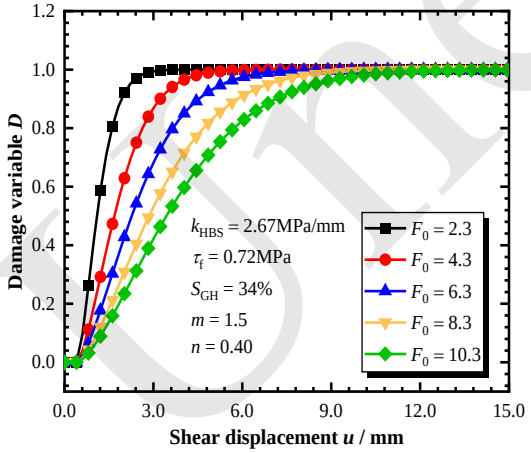


(b) Damage variable curves

**Fig. 10 Influence of model parameter $F_0$ on the shear response curves and damage evolution of GHBS.**

## 5.2 The influence of *m*

The influence of the distribution parameter $m$ on shear stress-shear displacement curves and damage evolution inside GHBS is depicted in Fig. 11. Fig. 11a shows the distribution parameter $m$ does not have any effect on the linear elastic deformation stage of GHBS. Note that the larger the distribution parameter $m$, the smaller the shear stress when entering the strain softening stage. At the same time, the shear stress-shear displacement curves show a tendency for a transition from ductile to brittle failure as the distribution parameter $m$ increases. Microscopic perspectives, such as the damage evolution of GHBS in terms of deformation, can be used to understand the above findings. Fig. 11b shows there is a transition point $T$. GH-bearing sediments with a larger distribution parameter $m$ are less likely to suffer bonding failure prior to the transition point $T$ than those with a smaller distribution parameter $m$ after passing over the transition point $T$.

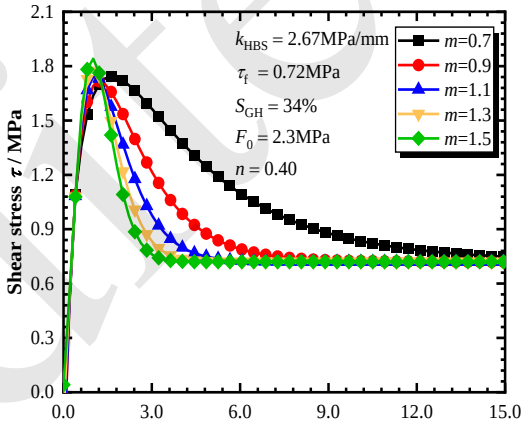


(a) Shear stress-displacement curves

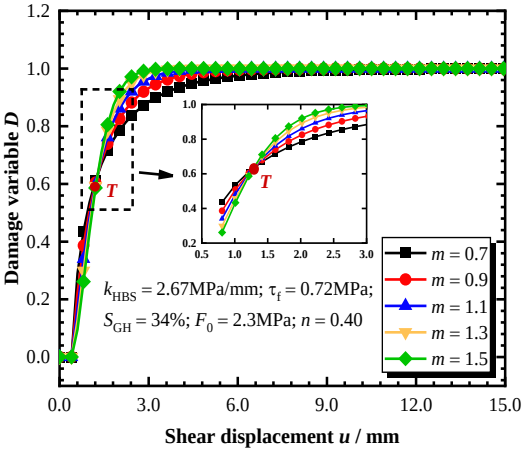


(b) Damage evolution curves

**Fig. 11 Effect of distribution parameter $m$ on the shear response curves and damage evolution of GHBS.**

## 6 Discussion

GH-bearing sediments are inhomogeneous geotechnical materials consisting of GH particles and

soil particles. Published studies have demonstrated that the cementation failure between soil particles and GH particles inside GHBS is the microscopic origin of the macroscopic deformation and failure processes (Wu et al., 2020). Therefore, investigating damage evolution will contribute to revealing the microscopic deformation mechanisms of GHBS during the shearing process. The evolution equation of damage variable $D$ may be obtained from Eq. (8), and the evolution equation of the damage rate $R_D$ can be derived as follows:

$$R_D = \frac{\mathrm{d}D}{\mathrm{d}u} = \frac{mk_{\mathrm{HBS}}\left(k_{\mathrm{HBS}}u - \sigma_{\mathrm{n}}\tan\varphi_{\mathrm{HBS}}^{\mathrm{y}} - c_{\mathrm{HBS}}^{\mathrm{y}}\right)^{m-1}}{F_0^m} \exp\left[-\left(\frac{k_{\mathrm{HBS}}u - \sigma_{\mathrm{n}}\tan\varphi_{\mathrm{HBS}}^{\mathrm{y}} - c_{\mathrm{HBS}}^{\mathrm{y}}}{F_0}\right)^m\right]. \tag{34}$$

Fig. 12 depicts the total shear stress, shear stress of the bonded elements, shear stress of the frictional elements, damage variables, and damage rate plotted against the shear displacements for GHBS. According to the development of shear stress, as described in the first section, the total shear stress-shear displacement curves can be divided into four stages. In stage AB, the shear stress of bonded elements is equal to the total shear stress, while the shear stress of frictional elements is near zero, indicating that the total shear stress is supported completely by bonded elements. When entering the yield hardening stage, the shear stress borne by the frictional elements increases rapidly, while the shear stress growth rate of bonded elements decreases. This indicates that irreversible plastic deformation occurs inside GHBS and bonded elements and frictional elements bear the total shear stress jointly. After passing the peak point C, the shear stress of the bonded elements rapidly decreases while the shear stress of the frictional elements continues to increase. When the shear displacement exceeds a certain threshold, the shear stress of the frictional elements begins to exceed the shear stress of the bonded elements. Before this threshold, the bonded elements dominate the macroscopic strength and deformation of GHBS, while after this point the frictional elements play a dominant role in the mechanical behavior of GHBS. Finally, the shear stress of the bonded elements decreases to zero whereas the shear stress of the frictional elements increases until it is equal to the total shear stress. It then remains constant when entering stage DE, indicating that the shear resistance of frictional elements provides the residual strength of GH-bearing sediments after destruction.

Fig. 12 shows the damage evolution and damage rate evolution process inside GH-bearing sediments. The damage rate evolution pattern is a convex parabolic curve, as shown in the graph, whereas the total damage evolution curve within GH-bearing sediments has an S-shape. The damage evolution curve inside GHBS may be separated into four stages based on damage rate evolution:

(1) Undamaged stage: damage variable $D$, and damage rate $R_{\mathrm{D}}$ are all equal to zero and remain unchanged, indicating that there is no hydrate bond breakage between GH particles and sand particles, corresponding to the elastic deformation stage of the shearing process.

(2) Acceleration damage stage: the increase in damage rate leads to a rapid accumulation of damage inside GHBS, which means that a lot of hydrate bond breakage occurs during the shearing process. In addition, when compared to the second stage of the shear deformation process, the rapid increase in damage rate is strongly related to the shear yielding of GHBS.

(3) Damage accumulation stage: the damage rate reaches the peak point and gradually begins to decrease with increasing shear displacements, while the accumulation of damage inside GHBS continues to increase in this stage. Note that the peak point of the damage rate curve occurs earlier than that of the shear stress curve. These findings agree with those from previous discrete element investigations and might be related to the development of shear bands.

(4) Stabilization stage: the damage rate inside GH-bearing sediments decreases to zero, while the damage variable approaches 1, after which it stops changing. This shows that the hydrate cementation in the shear bands has suffered complete breakage, enabling gas hydrate particles to enter the pore spaces, and the shear resistance between sand particles and GH particles provides residual strength.

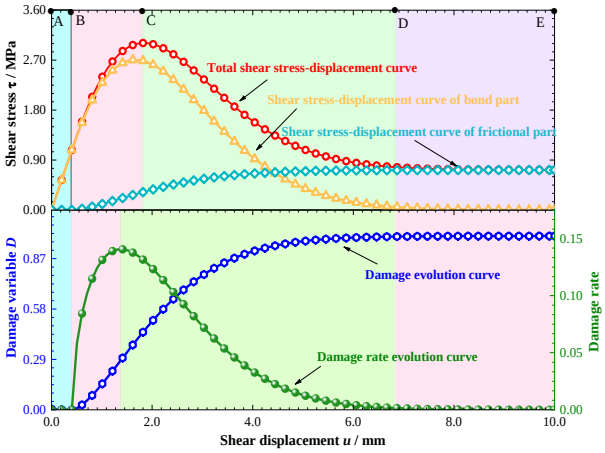


**Fig. 12 Shear stress partition and damage evolution of GHBS under shearing process.**

## 5 Conclusions

In this paper, to predict the deformation and failure process of GHBS in direct shear tests, a novel shear damage model based on homogenization theory and modified M-C criterion is suggested. The quality and validity of the shear damage model was evaluated against representative direct shear test results. The following conclusions can be drawn from the analysis:

1. The novel shear damage model can predict the deformation and failure characteristics, especially strain softening characteristics due to bond breakage of GH, by introducing the damage mechanics. By comparing the experimental and theoretical results, the global performance of the novel shear damage model was shown to be satisfactory.
2. The distribution parameter $F_0$ reflects mainly the statistical average macroscopic strength, while the distribution parameter $m$ affects mainly the post-peak morphology of GHBS. The shape of the whole shear stress-shear displacements curves of GHBS is determined by the GH saturation and normal pressure, which is reflected by the conjugacy of $F_0$ and $m$.
3. The shear damage model proposed in this study can better describe the damage evolution and shear stress partition mechanisms inside GHBS during the shearing process. Additionally, it reveals the cross-scale relationship between microscopic damage evolution, mesoscopic stress partition, and macroscopic mechanical behavior. Consequently, it can more accurately reflect the nonlinear deformation and strain-softening characteristics of GH-bearing sediments.

The shear damage model proposed in this paper has been verified by experimental data of GH-bearing sediments with less than 50% saturation. In the future, other direct shear test data of GHBS with more than 50% saturation need to be adopted to evaluate the performance of the shear damage model. Additionally, it is well-known that heterogeneity is a key feature of clayey-silty GHBS found in the South China Sea. Ren et al. (2022a and 2022b) reported that GH is first generated in small pores and then grows in large voids, resulting in heterogeneity in the spatial distribution of GH. At the same time, several studies using experiments and numerical simulation have demonstrated the important effect of the heterogeneity of particle distribution on the mechanical characteristics of GHBS (Zhang et al., 2022; Masui et al., 2005; Hyodo et al., 2017). In the present shear damage model, only GH hydrate saturation was considered, not hydrate morphology and structural heterogeneity. In our ongoing work, we will attempt to capture the effect of hydrate morphology, fine content and structural heterogeneity on the elastic properties and plastic deformation based on the meso-mechanics theory of the composite material.

## Acknowledgments

This work was supported by the Independent Innovation Research Program of China University of Petroleum (East China) (Grant No. 27RA2215005)

## Author contributions

Hui Wang designed the research and wrote the first draft of the manuscript. Bo Zhou revised and edited the final version.

## Conflict of interest

Hui Wang and Bo Zhou declare that they have no conflict of interest.

## References

Bai B, Zhou R, Yang G, et al., 2023. The constitutive behavior and dissociation effect of hydrate-bearing sediment within a granular thermodynamic framework. *Ocean Engineering*, 268:113408. https://doi.org/10.1016/j.oceaneng.2022.113408

Brugada J, Cheng YP, Soga K, et al., 2010. Discrete element modeling of geo-mechanical behavior of gas hydrate soils

with pore-filling hydrate distribution. *Granular Matter*, 12(5): 517-525. https://doi.org/10.1007/s10035-010-0210-y

Chaouachi M, Falenty A, Sell K, et al., 2015. Microstructural evolution of gas hydrates in sedimentary matrices observed with synchrotron X-ray computed tomographic microscopy. *Geochemistry, Geophysics, Geosystems*, 16:1711-1722. https://doi.org/10.1002/2015GC005811.

Deusner C, Gupta S, Xie XG, et al., 2019. Strain rate-dependent hardening-softening characteristics of gas hydrate-bearing sediments. *Geochemistry, Geophysics, Geosystems*, 20(11): 4885-4905. https://doi.org/10.1029/2019GC008458

Dong L, Li Y, Liao H, et al., 2020. Strength estimation for hydrate-bearing sediments based on triaxial shearing tests. *Journal of Petroleum Science and Engineering*, 184: 106478. https://doi.org/10.1016/j.petrol.2019.106478

Farahani MV, Hassanpouryouzband A, Yang J, 2021. Insights into the climate-driven evolution of gas hydrate-bearing permafrost sediments: Implications for prediction of environmental impacts and security of energy in cold regions. *RSC Advances*, 11(24): 14334-14346. https://doi.org/10.1039/D1RA01518D

Farahani MV, Hassanpouryouzband A, Yang J, et al., 2021. Development of a coupled geophysical-geothermal scheme for quantification of hydrates in gas hydrate-bearing permafrost sediments. *Physical Chemistry Chemical Physics*, 23(42): 24249-24264. https://doi.org/10.1039/D1CP03086H.

Hallinan Jr A J, 1993. A review of the Weibull distribution. *Journal of Quality Technology*, 25(2): 85-93. https://doi.org/10.1080/00224065.1993.11979431

Hou G, Liang D, Li X., 2018. Experimental study on hydrate anti-agglomeration in the presence of rhamnolipid. *RSC Advances*, 8(69): 39511-39519. https://doi.org/10.1039/C8RA07215A

Hyodo M, Li Y, Yoneda J, et al., 2013. Mechanical behavior of gas-saturated gas hydrate-bearing sediments. *Journal of Geophysical Research: Solid Earth*, 118(10): 5185-5194. https://doi.org/10.1002/2013JB010233

Hyodo M, Li Y, Yoneda J, et al., 2014. Effects of dissociation on the shear strength and deformation behavior of gas hydrate-bearing sediments. *Marine and Petroleum Geology*, 51: 52-62. https://doi.org/10.1016/j.marpetgeo.2013.11.015

Hyodo M, Wu Y, Nakashima K, et al., 2017. Influence of fines content on the mechanical behavior of gas hydrate-bearing sediments. *Journal of Geophysical Research: Solid Earth*, 122(10): 7511-7524. https://doi.org/10.1002/ 2017JB014154

Hyodo M, Yoneda J, Yoshimoto N, et al., 2013. Mechanical and dissociation properties of gas hydrate-bearing sand in deep seabed. *Soils and Foundations*, 53(2): 299-314. https://doi.org/10.1016/j.sandf.2013.02.010

Ji Y, Hou J, Cui G, et al., 2019. Experimental study on gas hydrate formation in a partially saturated sandstone using low-field NMR technique. *Fuel*, 251: 82-90. https://doi.org/10.1016/j.fuel.2019.04.021

Jia Y, Zhu C, Liu L, Wang D. Marine geohazards: review and future perspective. *Acta Geologica Sinica- English Edition*, 2016; 90(4): 1455-1470. https://doi.org/10.1111/1755-6724.12779

Jiang M, Chen H., Tapias M, et al., 2014. Study of mechanical behavior and strain localization of gas hydrate-bearing sediments with different saturations by a new dem model. *Computers and Geotechnics*, 57: 122-138. https://doi.org/10.1016/j.compgeo.2014.01.012

Jiang M, Liu J, Shen Z, 2019. DEM simulation of grain-coating type gas hydrate bearing sediments along various stress paths. *Engineering Geology*, 261(105280): 1-13. https://doi.org/10.1016/j.enggeo.2019.105280

Kajiyama S, Hyodo M, Nakata Y, et al., 2017. Shear behaviour of gas hydrate bearing sand with various particle characteristics and fines. *Soils and Foundations*, 57(2): 176-193. https://doi.org/10.1016/j.sandf.2017.03.002

Kvenvolden KA, 1998. A primer on the geological occurrence of gas hydrate. *Geological Society, London, Special Publications*, 137(1): 9-30. https://doi.org/10.1144/GSL.SP.1998.137.01.02

Kvenvolden KA, 1999. Potential effects of gas hydrate on human welfare. *Proceedings of the National Academy of Sciences of the United States of America*, 96(7): 3420-3426. https://doi.org/10.1073/pnas.96.7.3420

Lei L, Seol Y, Choi JH, et al., 2019. Pore habit of methane hydrate and its evolution in sediment matrix–Laboratory visualization with phase-contrast micro-CT. *Marine and Petroleum Geology*, 104: 451-467. https://doi.org/10.1016/j.marpetgeo.2019.04.004

Li C, Liu C, Hu G, et al., 2019. Investigation on the multiparameter of hydrate-bearing sands using nano-focus X-ray computed tomography. *Journal of Geophysical Research: Solid Earth*, 124(3): 2286-2296. https://doi.org/10.1029/2018JB015849

Li D, Wang Z, Liang D, et al., 2019. Effect of Clay Content on the Mechanical Properties of Hydrate-Bearing Sediments during Hydrate Production via Depressurization. *Energies*, 12(14): 1-14. https://doi.org/10.3390/en12142684

Liu Z, Wei H, Peng L, et al., 2017. An easy and efficient way to evaluate mechanical properties of gas hydrate-bearing sediments: The direct shear test. *Journal of Petroleum Science and Engineering*, 149: 56-64. https://doi.org/10.1016/j.petrol.2016.09.040

Liu, Z., Dai, S., Ning, F., et al., 2018. Strength estimation for hydrate-bearing sediments from direct shear tests of hydrate-bearing sand and silt. *Geophysical Research Letters*, 45: 715-723. https://doi.org/10.1002/2017GL076374

Luo T, Li Y, Madhusudhan BN, et al., 2020. Deformation behaviors of hydrate-bearing silty sediment induced by

depressurization and thermal recovery. *Applied Energy*, 276, 115468: 1-12. https://doi.org/10.1016/j.apenergy.2020.115468

Masui A, Haneda H, Ogata Y, et al., 2005. The effect of saturation degree of gas hydrate on the shear strength of synthetic gas hydrate sediments. *Proceedings of the 5th International Conference on Gas Hydrates, Trondheim, Norway*, 2037: 657-663.

Miyazaki K, Masui A, Sakamoto Y, et al., 2011. Triaxial compressive properties of artificial gas hydrate-bearing sediment. *Journal of Geophysical Research: Solid Earth*, 116(B6): 1-11. https://doi.org/10.1029/2010JB008049

Miyazaki K, Tenma N, Aoki K, et al., 2012. A nonlinear elastic model for triaxial compressive properties of artificial methane-hydrate-bearing sediment samples. *Energies*, 5(10): 4057-4075. https://doi.org/10.3390/en5104057

Ng CWW, Baghbanrezvan S, Kadlicek T, et al., 2020. A state-dependent constitutive model for methane hydrate-bearing sediments inside the stability region. *Géotechnique*, 70(12): 1094-1108. https://doi.org/10.1680/jgeot.18.P.143

Ng CWW, Lau SY, Zhang Q, et al., 2023. A state-dependent constitutive model for gas hydrate-bearing sediment incorporating phase change. *Gas Science and Engineering*, Volume 119, 205102. https://doi.org/10.1016/j.jgsce.2023.205102

Pinkert S, 2017. Rowe's stress-dilatancy theory for hydrate-bearing sand. *International Journal of Geomechanics*, 17(1): 1-5. https://doi.org/10.1061/(ASCE)GM.1943-5622.0000682

Pinkert S, Grozic J, Priest JA, 2015. Strain-softening model for hydrate-bearing sands. *International Journal of Geomechanics*, 15(6): 04015007. https://doi.org/10.1061/(ASCE)GM.1943-5622.0000477

Ren J, Liu X, Niu M, et al., 2022a. Effect of sodium montmorillonite clay on the kinetics of $CH_4$ hydrate- implication for energy recovery. *Chemical Engineering Journal*, 437, 135368. https://doi.org/10.1016/j.cej.2022.135368

Ren J, Yin Z, Li Q, et al., 2022b. Pore-scale investigation of CH4 hydrate kinetics in clayey-silty sediments by Low-Field NMR. *Energy & Fuels*, 36(24): 14874-14887. https://doi.org/10.1021/acs.energyfuels.2c03255

Skempton A W, 1985. Residual strength of clays in landslides, folded strata and the laboratory. *Geotechnique*, 35(1): 3-18. https://doi.org/10.1680/geot.1985.35.1.3

Sloan ED, 2003. Fundamental principles and applications of natural gas hydrates. *Nature*, 426 (6964): 353-363.

Sloan ED, Koh CA, 2007. Clathrate hydrates of natural gases. *CRC Press*.

Song Y, Wang S, Yang M, et al., 2015. MRI measurements of $CO_2$-$CH_4$ hydrate formation and dissociation in porous media. *Fuel*, 140(15): 126-135. https://doi.org/10.1016/j.fuel.2014.09.086

Song Y, Zhu Y, Liu W, et al., 2016. The effects of gas hydrate dissociation at different temperatures on the stability of porous sediments. *Journal of Petroleum Science and Engineering*, 147: 77-86. https://doi.org/10.1016/j.petrol.2016.05.009

Stern LA, Kirby SH, Durham WB, 1997. Polycrystalline gas hydrate: synthesis from superheated ice, and low-temperature mechanical properties. *Energy & Fuels*, 12(2): 201-211. https://doi.org/10.1021/ef970167m

Uchida S, Xie X, Leung Y, 2016. Role of critical state framework in understanding geomechanical behavior of gas hydrate-bearing sediments. *Journal of Geophysical Research: Solid Earth*, 121(8): 5580-5595. https://doi.org/10.1002/2016JB012967

Wang H, Chen Y, Zhou B, et al., 2021. Investigation of the effect of cementing ratio on the mechanical properties and strain location of hydrate-bearing sediments by using DEM. *Journal of Natural Gas Science and Engineering*, 94: 104123. https://doi.org/10.1016/j.jngse.2021.104123

Wang Y, Wang R, Yu J, et al., 2023. SPF-MHBS: a stress partition constitutive framework for methane hydrate-bearing sediments. *Acta Geotechnica*, 18(4), 1919-1944. https://doi.org/10.1007/s11440-022-01621-6

Wu P, Li Y, Liu W, et al., 2020. Cementation failure behavior of consolidated gas hydrate-bearing sand. *Journal of Geophysical Research: Solid Earth*, 125(1): 1-19. https://doi.org/10.1029/2019JB018623

Wu P, Wang H, Huang L, et al., 2023. Pore-scale analysis of hydrate saturation on the physical parameters of hydrate-bearing sediment with different particle shapes. *Gas Science and Engineering*, 205052. https://doi.org/10.1016/j.jgsce.2023.205052

Xie S, Lin H, Chen Y, et al., 2020a. A damage constitutive model for shear behavior of joints based on determination of the yield point. *International Journal of Rock Mechanics and Mining Sciences*, 128(104269): 1-12. https://doi.org/10.1016/j.ijrmms.2020.104269

Xie S, Lin H, Wang Y, et al., 2020b. A statistical damage constitutive model considering whole joint shear deformation. *International Journal of Damage Mechanics*, 29(6): 988-1008. https://doi.org/10.1177/1056789519900778

Xu JL, Wang R, Xu CS, et al., 2023. Application and improvement of a stress partition framework-based methane hydrate-bearing sediment constitutive model for wide range confining stress. *Computers and Geotechnics*, 159(105463): 1-14. https://doi.org/10.1016/j.compgeo.2023.105463

Xu M, Song E, Jiang H, et al., 2016. DEM simulation of the undrained shear behavior of sand containing dissociated gas hydrate. *Granular Matter*, 18(4): 1-13. https://doi.org/10.1007/s10035-016-0675-4

Yan C, Cheng Y, Li M, et al., 2017. Mechanical experiments and constitutive model of natural gas hydrate reservoirs.

*International Journal of Hydrogen Energy*, 42(31): 19810-19818.
https://doi.org/10.1016/j.ijhydene.2017.06.135

Yang M, Song Y, Jiang L, et al., 2014. Hydrate-based technology for $CO_2$ capture from fossil fuel power plants. *Applied Energy*, 116(3): 26-40.
https://doi.org/10.1016/j.apenergy.2013.11.031

Yoneda J, Jin Y, Katagiri J, et al., 2016. Strengthening mechanism of cemented hydrate-bearing sand at microscales. *Geophysical Research Letters*, 43(14): 7442-7450.
https://doi.org/10.1002/2016GL069951

Yoneda J, Masui A, Konno Y, et al., 2015. Mechanical properties of hydrate-bearing turbidite reservoir in the first gas production test site of the Eastern Nankai Trough. *Marine and Petroleum Geology*, 66: 471-486.
https://doi.org/10.1016/j.marpetgeo.2015.02.029

Yu F, Song Y, Liu W, et al., 2011. Analyses of stress-strain behavior and constitutive model of artificial gas hydrate. *Journal of Petroleum Science and Engineering*, 77(2): 183-188.
https://doi.org/10.1016/j.petrol.2011.03.004

Yun TS, Santamarina JC, Ruppel C, 2007. Mechanical properties of sand, silt, and clay containing tetrahydrofuran hydrate. *Journal of Geophysical Research: Solid Earth*, 112(B4): 1-13.
https://doi.org/10.1029/2006JB004484

Zhang N, Wang HN, Jiang MJ, 2022. A mesoelastic-plastic damage model for hydrate-bearing sediments with various hydrate-growth patterns. *Ocean Engineering*, 266(112919): 1-20.
https://doi.org/10.1016/j.oceaneng.2022.112919

Zhang X, Lin J, Lu X, et al., 2018. A hypoplastic model for gas hydrate-bearing sandy sediments. *International Journal for Numerical and Analytical Methods in Geomechanics*, 42(7): 931-942.
https://doi.org/10.1002/nag.2772

Zhang J, Liu X, Chen D, et al., 2022. An investigation on the permeability of hydrate-bearing sediments based on pore-scale CFD simulation. *International Journal of Heat and Mass Transfer*, 192, 122901.
https://doi.org/10.1016/j.ijheatmasstransfer.2022.122901.

Zhou M, Soga K, Yamamoto K, 2018. Upscaled anisotropic gas hydrate critical state model for turbidite hydrate-bearing sediments at east Nankai trough. *Journal of Geophysical Research: Solid Earth*, (5): 6277-6298.
https://doi.org/10.1029/2018JB015653

Zhu CQ, Zhang M, Liu X, et al., 2017. Gas hydrates: Production, geohazards and monitoring. *Journal of Catastrophology*, 32(3): 1-8.http://doi.org/ 10.3969/j.issn.1000-811X.2017.03.010

Zou Z, Yan J, Tang H, et al., 2020. A shear constitutive model for describing the full process of the deformation and failure of slip zone soil. *Engineering Geology*, 276(105766): 1-11.
https://doi.org/10.1016/j.enggeo.2020.105766.

## 中文概要

**题　目：** 一种描述水合物沉积物剪切变形破坏过程的新型剪切损伤模型

**作　者：** 王辉[1,2]，周博[1]

**机　构：** [1]中国石油大学(华东)，储运与建筑工程学院，中国青岛，266580；[2]武汉大学，水工程科学研究院中国武汉，430072；

**目　的：** 水合物开采造成的水合物饱和度降低严重影响了水合物储层的宏观力学响应，造成储层失稳，海底滑坡等灾害。本文旨在基于水合物沉积物的微观变形机制提出可以考虑水合物含量影响的水合物沉积物的剪切损伤本构模型。

**创新点：** 1.基于均匀化理论和修正摩尔-库伦准则，提出了水合物沉积物的剪切损伤本构模型；2. 采用该模型研究了模型参数的物理意义和水合物沉积物剪切变形破坏的细观机制。

**方　法：** 1.通过分析水合物沉积物剪切变形的微观机制，基于均匀化理论建立了水合物沉积物的剪应力分配方程；2. 基于统计损伤力学和考虑水合物饱和度的修正摩尔-库仑强度准则，建立了水合物沉积物的剪切损伤本构模型；3. 通过将理论预测结果与试验结果对比，验证所提出模型的可行性和有效性。

**结　论：** 1. 该剪切损伤模型通过引入损伤力学，可以预测水合物沉积物的变形破坏特征，特别是水合物胶结破坏引起的应变软化特征。实验结果与理论结果比较表明，该剪切损伤模型能够较好地模拟水合物沉积物的剪切应力−剪切位移曲线全过程；2. 分布参数 $F_0$ 主要反映水合物沉积物的统计平均宏观强度，而分布参数 $m$ 主要影响水合物沉积物剪切应力曲线的峰后形态；3. 本研究提出的剪切损伤模型能够更好地描述剪切过程中水合物沉积物内部的损伤演化和剪应力分配机制。揭示了细观损伤演化、细观应力分配与宏观力学行为之间的跨尺度关系。因此，该方法能更准确地反映含天然气水合物沉积物的非线性变形和应变软化特征。

**关键词：** 水合物沉积物；剪切损伤模型；均匀化理论；修正摩尔-库伦模型；损伤演化